EuroGNC Navigation Guidance Control CEAS Bristol, UK June 11th-13th 2024
University of BRISTOL ROYAL AERONAUTICAL SOCIETY AIAA

A vision-based control solution for autonomous approach and landing of an airliner

Sofiane Kraïem Research Engineer, ONERA - The French Aerospace Lab, Information Processing and Systems Department, 31000, Toulouse, France. sofiane.kraiem@onera.fr

Mario Cassaro Research Engineer, ONERA - The French Aerospace Lab, Information Processing and Systems Department, 31000, Toulouse, France. mario.cassaro@onera.fr

Cédric Seren Research Engineer, ONERA - The French Aerospace Lab, Information Processing and Systems Department, 31000, Toulouse, France. cedric.seren@onera.fr

Aurélien Plyer Research Engineer, ONERA - The French Aerospace Lab, Information Processing and Systems Department, 91123, Palaiseau, France. aurelien.plyer@onera.fr

Gustav Öman Lundin Research Engineer, ONERA - The French Aerospace Lab, Information Processing and Systems Department, 31000, Toulouse, France. gustav.oman_lundin@onera.fr

Mathieu Brunot Research Engineer, Airbus, 31000, Toulouse, France. mathieu.brunot@airbus.com

ABSTRACT

In the strive for always more safe and autonomous operations for civil aviation the landing phase remains by far the most challenging. Robustifying the already existing automatic landing system, classically based on external infrastructure, with vision-based solutions have recently demonstrated promising perspectives. Nonetheless, the design and validation of such novel algorithms comes at enormous costs and logistic effort for installation, in-flight data collection and testing. This paper introduces a novel Pose-Based Visual Servoing (PBVS) approach for autonomous landing. The proposed method separates the guidance laws from the image flow processing to leverage already certified autopilots. Through computer vision algorithms, a vision-aided Extended Kalman Filter (EKF) receives visual measurements, based on the knowledge of geographical coordinates of some objects of interest, enabling the estimation of the aircraft's pose with respect to a designated runway. The control framework is implemented for a detailed Boeing 747 model on a real-time simulation platform, which accurately replicates various weather and visual conditions worldwide. The feasibility and performance of the control strategy are evaluated through numerous landings at Toulouse airport, encompassing a range of initial and flight conditions.

Keywords: Autonomous vehicles, Computer Vision (CV), Image Processing Algorithms (IPA), Multisensor Data Fusion (MDF), Adaptive Extended Kalman Filtering (AEKF)

1 Introduction

Automatic landing represents an advantageous solution for reducing pilot workload and addressing challenging operational conditions, such as crosswinds or limited visibility. This is why Airbus is committed to developing new solutions to further enhance the capabilities of autonomous land-

ing, including technologies like the Satellite Based Augmentation System (SBAS) [1]. The introduction of new solutions enhancing performances is primarily motivated by improving the safety. As depicted in Fig. 1, the average fatal accident rate has demonstrated a decline with the introduction of new aircraft (A/C) generations. The initial generation was constrained by analog electronic systems prevalent during that period. The second generation saw advancements in autoflight and autothrottle systems, resulting in an immediate halving of the average fatal accident rate. The third generation introduced digital technologies, incorporating Flight Management Systems (FMS) and Navigation Displays (ND) that enhanced navigation capabilities and positioning awareness. The integration of terrain awareness and warning systems further contributed to a reduction in controlled flight into terrain accidents. The latest generation, inaugurated with the Airbus A320 model in 1988, introduced electrical flight control systems, commonly referred to as Fly-By-Wire (FBW). These technological leaps provided new means of safeguarding the aircraft's flight envelope and enhancing the performance and robustness of the Guidance, Navigation, and Control (GNC) systems, thereby mitigating the risk of in-flight loss of control accidents [2]. As a result, the 10-year moving average of the fatal accident rate for the fourth aircraft generation has plummeted to 0.05 in 2022, signifying that approximately 20 million flights must be completed to observe a single fatal accident occurrence.

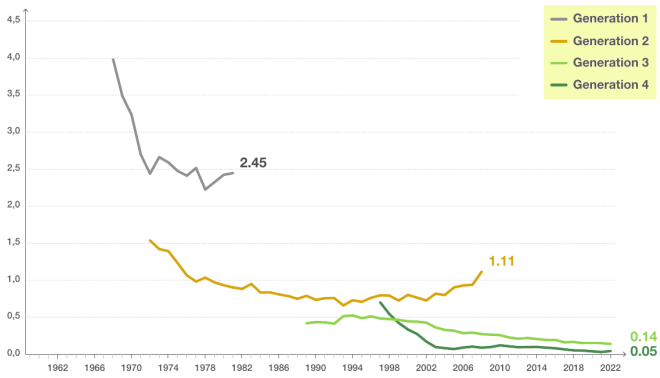

Fig. 1 Ten years moving average fatal accident rate (per million flights) per A/C generation. (Source: Airbus - https://accidentstats.airbus.com)

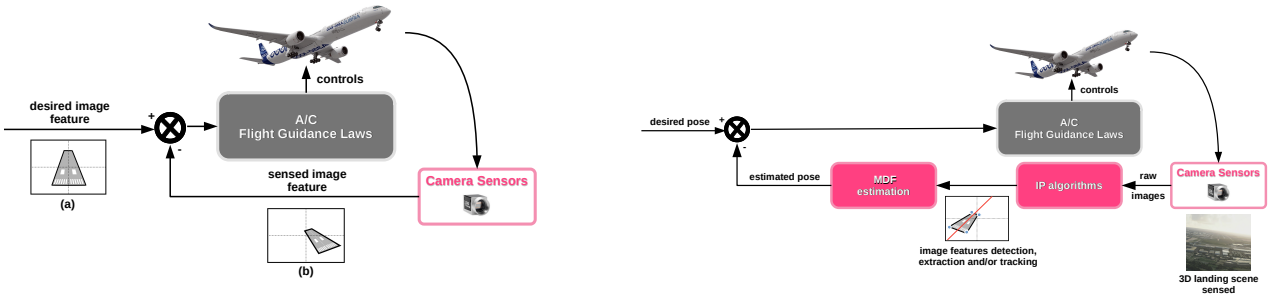

(a) Image Based Visual Servoing 2D principles **(b) Pose Based Visual Servoing 3D principles**

Fig. 2 Illustration of principal visual-based control strategies

Among the different flying phases of an A/C, the landing remains the most challenging one. Recent studies have focused on finding new robust approaches to either assist pilots or safely and autonomously land a fixed wing A/C. Beyond currently employed technologies such as Instrument Landing System (ILS) and Ground-Based Augmentation landing System (GBAS), different alternative systems based on on-board exteroceptive sensors are being designed and tested to expand autonomous landing capabilities to runways that lack equipped infrastructure. Working towards this end, embeddable vision sensors have emerged as a natural and affordable technological solution capable of providing new extra and dissimilar information for aircraft pose estimation relative to the ground. Visual servoing consists in using a vision sensor and computer vision algorithms in order to control the motion of the system [3]. Two control strategies can be distinguished, the Pose Based Visual Servoing (PBVS) and the Image Based Visual Servoing (IBVS). The principles of IBVS and PBVS are presented in Fig. 2 and extensively explained in references [3, 4]. In IBVS, the guidance objectives are directly formulated in the image plane, whereas in PBVS, vision serves as a means to estimate the vehicle's pose w.r.t the desired target,

and the image processing is separated from the control law. Remarkably, in the case of IBVS, knowledge of the aircraft's pose is not required. This characteristic confers a high level of robustness upon 2D visual servoing, particularly in relation to camera calibration. During the approach and landing phases of an A/C, Fig. 2a exemplifies the guidance objectives. The current image perception (b) must match the desired image feature (a), wherein the destination runway should be centered and exhibit symmetry. Although robust, IBVS solutions suffer however from a well-known problem: the generation of unsuitable and even singular 3D trajectories. To address this issue, it becomes necessary to separate the translation and rotation movements. Several techniques have been explored in the literature [5, 6]. Moreover, constrained IBVS approaches were also developed to guarantee that the visual primitive(s) or the target object(s) always remain observable i.e. inside camera Field Of Views (FOVs) [7, 8]. Other IBVS approaches focus on directly regulating the dynamics of visual information within the image, rather than the dynamics of the system itself. These methods are referred to as d2D/dt visual servoing. These approaches effectively address the absence of velocity measurements and do not focus on specific visual primitives or target objects within the image. Instead, they rely on optical flow data to control both the system's speed and its distance to the surrounding environment [9, 10]. For fixed-wing aircraft landing, nonlinear IBVS control strategies have been designed based on line primitives and proposed in several bibliographical references [11–15]. Serra et al. [15] introduced a robust nonlinear image-based controller designed for the flare phase of the landing maneuver. This controller is capable of handling wind disturbances by employing normalized Plücker coordinates to align the 2D line features of the runway edges in the image, thereby ensuring proper alignment of the A/C with the runway. Similarly, Coutard et al. [16] and Gibert and Puyou [17] addressed fixed-wing aircraft landing by designing IBVS controllers whose input signals correspond to both destination runway center-line and touchdown point coordinates. In comparison to the work presented in [16], [17] examines and verifies a novel set of visual features to address coupling and nonlinear effects, resulting in an overall improvement of performance of the IBVS control scheme. While IBVS schemes exhibit attractive robustness, implementing them for autonomous landing of large transport civil jet A/C necessitates the creation of an entirely new guidance law structure. This may pose a significant challenge in terms of certification by regulatory authorities, given the innovative nature of the approach. Moreover, IBVS solutions cause extra costs and maintenance efforts. For these reasons, the utilization of already certified guidance laws is a crucial consideration for A/C manufacturers. Currently, they are more inclined to explore PBVS solutions as a viable option. The primary benefit offered by PBVS lies in the separation of the control law from the aircraft's pose estimation relative to a target, achieved through the extraction of all pertinent visual primitives. However, when compared to IBVS approaches, PBVS demands a greater amount of prior knowledge regarding the captured 3D scene, such as navigation databases and camera calibrations. After the pioneering work led by Dickmanns et al. in dynamic vision for large size A/C and helicopters using multiple sensor data for state estimation [18, 19], Gibert et al. [20, 21] conducted comprehensive research on the development of various nonlinear observers for visually estimating flight-path deviations in the context of civil A/C landing applications. Their analysis of the observability of the nonlinear system in the estimation problem led to the conclusion that it is necessary to incorporate data from at least two points on the runway or its two sidelines in order to maintain system observability during the landing phase. Gibert [22] presented a comparison of up to six types of nonlinear observers. It is important to note that the available information includes aircraft attitude, ground-relative velocities, and accelerations, which are provided by the Inertial Measurement Unit (IMU) sensors. Notably, no geometric information related to the destination runway is necessary for the analysis. Further recent studies have considered Multisensor Data Fusion (MDF) techniques between a stereo camera and GPS/GNSS or an hybridization with inertial information, as well as solutions merging additional thermal sensors [23–26]. As presented in [27], time delays are systematically introduced by the image processing software layer that will affect any downstream estimation process. In the recent Europe-Japan collaborative research project called VISION [1], vision-based aircraft relative navigation to destination runways with known dimensions has

[1]VISION: Validation of Integrated Safety-enhanced Intelligent flight cONtrol

been tackled [23]. They developed a delayed-Error-State Kalman Filter which compensates, forward in time, for the image processing delay by using camera trigger signal.

In this paper, a novel PBVS strategy capable of ILS-like measurements and performance is developed. A Vision-Aided EKF (VAEKF) algorithm is introduced to estimate, at least partially, system state variables. This estimation stage is fed by one or several vision-based measurements elaborated by a set of Image Processing (IP) algorithms which aim at extracting all visual primitives of interest. The vision-based estimated states are used to reconstruct the standardized ILS error signals, which are then fed into the system guidance controllers. This can be done thanks to specific navigation database typically accessible through the Flight Management System. The proposed vision-based autonomous landing solution is validated on a high fidelity simulator with real-time constraints developed at ONERA [28].

The paper is structured as follows: Section 2 provides an overview of the overall control framework and details the image processing algorithms; Section 3 presents the VAEKF and the integration of chosen visual measurements in the estimation process; Section 4 assesses the system's performance by conducting landings on a real-time simulation platform that can replicate a range of visual and weather conditions. Finally, Section 5 concludes the article and states future perspectives.

2 Pose-Based Visual Servoing strategy

In this section, we introduce a vision-based autonomous landing control strategy. This approach offers an alternative solution for conducting autonomous landings without ILS and/or G/SBAS augmentation. To this end, we adopt a Pose-Based Visual Servoing (PBVS) approach. The concept is to incorporate supplementary measurements, either for the entire landing procedure or a specific timeframe, in order to enable an ILS-like landing to be autonomously executed. An overview of the control principle is first presented, then the IP and Computer Vision (CV) algorithms to provide a runway's center-line measurements are introduced. The novelty of the proposed PBVS approach lies in the selection of visual features and their integration into the process of estimating the aircraft's pose relative to the designated runway.

2.1 Overall principle

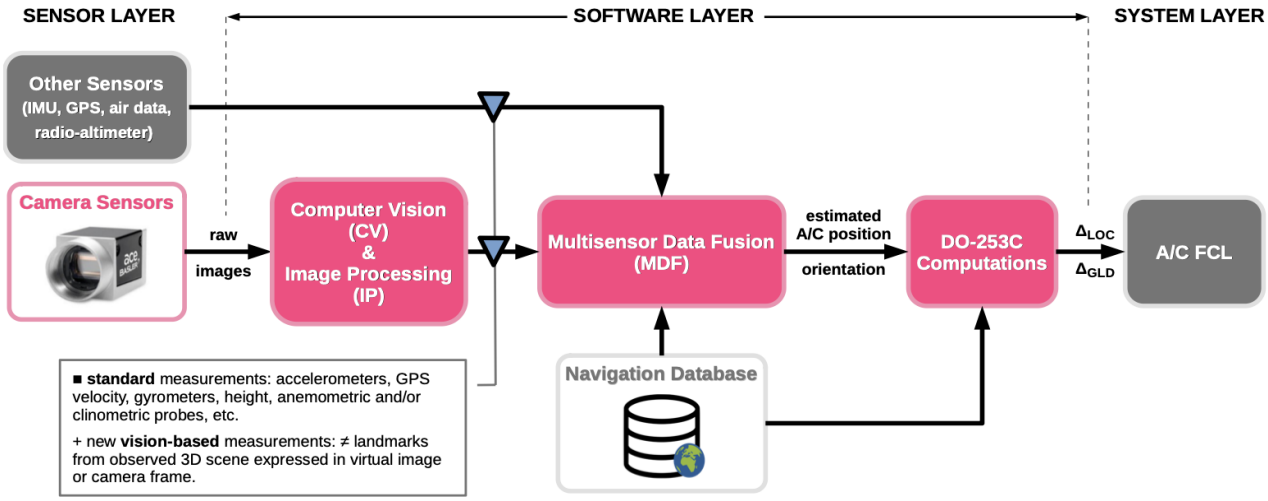

Fig. 3 General block diagram of the PBVS software solution.

The proposed PBVS strategy, depicted in Fig. 3, can be decomposed in: a sensor layer, a software layer and a system layer. The sensor layer is in charge of capturing all necessary raw data that guarantee to the global landing function a nominal behavior. The software layer aims at processing previous raw

data in order to deliver reliable flight-path deviations viewed as reference inputs by the downstream layer. This layer gathers both advanced image processing and the VAEKF algorithms, i.e. the MDF. The system layer can be any A/C autopilots to perform the final approach segment trajectory until the end of the landing flight phase. Such architecture presents several advantages. First, utilizing MDF algorithms that correlate all available measurements, it becomes feasible to filter out all signals processed by the CV+IP functional block. A crucial consideration arises from the fact that, in real-world scenarios, the noise characteristics of vision-based signals deviate from the assumptions of a normal density function. Raw IP measurements are frequently subject to non-stationary disturbances and can also exhibit a considerable number of outliers. This circumstance motivated the creation of an adaptive MDF algorithm designed to accommodate these particularities. Second, the system layer may be embodied by current A/C Flight Control Systems (FCS) directly, since upstream functional pipeline delivers the same flight-path deviations format (DEVLOC, DEVGLD) as for ILS-based autopilots. Using these physical-analytical redundant measurements as reference inputs for aircraft navigation and guidance does not question current commercial jet A/C control strategy entrenched in aviation industry. Third, for the MDF component, the potential of using model-based techniques for describing the expected A/C behavior. On the one hand, they permit to deliver filtered and consolidated flight-path deviation estimates by merging all available measurements (including the vision-based ones) in nominal (unfaulty) conditions, and, on the other hand, they can make up for failed measurement inputs in degraded (faulty) conditions.

Thus, the software layer reconstructs by merging all available inertial and vision-based measurements both lateral and vertical flight-path deviation estimates which can directly feed the A/C flight guidance control laws. This conversion is achieved by referring to the appendix C of DO-253 official document [29] written by the Radio Technical Commission for Aeronautics, now referred as RTCA. With an additional navigation database that gathers all necessary information related to many destination runways worldwide (glide path angle, threshold crossing-height, runway width and length, etc.), the lateral and vertical deviations flight-path deviations, respectively DEVLOC and DEVGLD, can be computed as:

$$\begin{cases} \mathsf{DEVLOC} = K_{\mathsf{LOC}} \tan^{-1}\left(\mathbf{u}_{\mathsf{lat}} \cdot \left(\mathbf{r}_{\mathsf{A/C}}^{\mathsf{ECEF}} - \mathbf{r}_{\mathsf{0,LOC}}^{\mathsf{ECEF}}\right) \middle| \mathbf{u}_{\mathsf{rwy}} \cdot \left(\mathbf{r}_{\mathsf{A/C}}^{\mathsf{ECEF}} - \mathbf{r}_{\mathsf{0,LOC}}^{\mathsf{ECEF}}\right) \right) & \text{(1a)} \\ \mathsf{DEVGLD} = K_{\mathsf{GLD}} \tan^{-1}\left(\mathbf{u}_{\mathsf{ver}} \cdot \left(\mathbf{r}_{\mathsf{A/C}}^{\mathsf{ECEF}} - \mathbf{r}_{\mathsf{0,GLD}}^{\mathsf{ECEF}}\right) d(\mathbf{r}_{\mathsf{A/C}}^{\mathsf{ECEF}}, \mathbf{r}_{\mathsf{0,GLD}}^{\mathsf{ECEF}})\right) - 0.7 & \text{(1b)} \\ d(\mathbf{r}_{\mathsf{A/C}}^{\mathsf{ECEF}}, \mathbf{r}_{\mathsf{0,GLD}}^{\mathsf{ECEF}}) = \sqrt{\left(\mathbf{u}_{\mathsf{rwy}} \cdot \left(\mathbf{r}_{\mathsf{A/C}}^{\mathsf{ECEF}} - \mathbf{r}_{\mathsf{0,GLD}}^{\mathsf{ECEF}}\right)\right)^2 + \left(\mathbf{u}_{\mathsf{lat}} \cdot \left(\mathbf{r}_{\mathsf{A/C}}^{\mathsf{ECEF}} - \mathbf{r}_{\mathsf{0,GLD}}^{\mathsf{ECEF}}\right)\right)^2} & \text{(1c)} \end{cases}$$

In Eq. (1a) and (1b), coefficients $(K_{\mathsf{LOC}}, K_{\mathsf{GLD}})$ correspond to constant quantities that are computed from the on board navigation database. The orthogonal triplet $(\mathbf{u}_{\mathsf{rwy}}, \mathbf{u}_{\mathsf{lat}}, \mathbf{u}_{\mathsf{ver}})$ defines the runway frame considered for these calculations whose origin coincides with destination runway Landing Threshold Point (LTP). It is a local East-North-Up (ENU) frame and the three axes are aligned alongside of the runway, to the left and upwards respectively. Then, $\mathbf{r}_{\mathsf{A/C}}^{\mathsf{ECEF}}$ refers to the position vector of the aircraft expressed in the ECEF frame. Both $\mathbf{r}_{\mathsf{0,LOC}}^{\mathsf{ECEF}}$ and $\mathbf{r}_{\mathsf{0,GLD}}^{\mathsf{ECEF}}$ vectors designate constant reference positions whose coordinates are also given in ECEF frame. They are computed using previous navigation database for any given destination runway and correspond to specific points located in the close vicinity of the runway.

2.2 Image Processing and Computer Vision algorithms

Integrating any available vision measurements within navigation-based MDF can be done in several different ways, depending if any mathematical modeling can be derived to describe vision variables time evolution. If they exist, such models associate these latter vision variables with dynamical navigation states that will be estimated within an adapted and tightly coupled version of [vision/navigation]-based EKF estimation scheme. By contrast, if such modelings cannot be derived, any available vision measurements will therefore only be used to correct predicted A/C navigation state vector as dissimilar sources

of information. Thus, all available vision measurements will bring an extra and dissimilar information that will be merged within the EKF-based estimation scheme. The concept revolves around generating a prediction based on the vision measurements of a runway center-line parametrization. This prediction serves to augment the innovation sequence utilized in the EKF for estimating aircraft states.

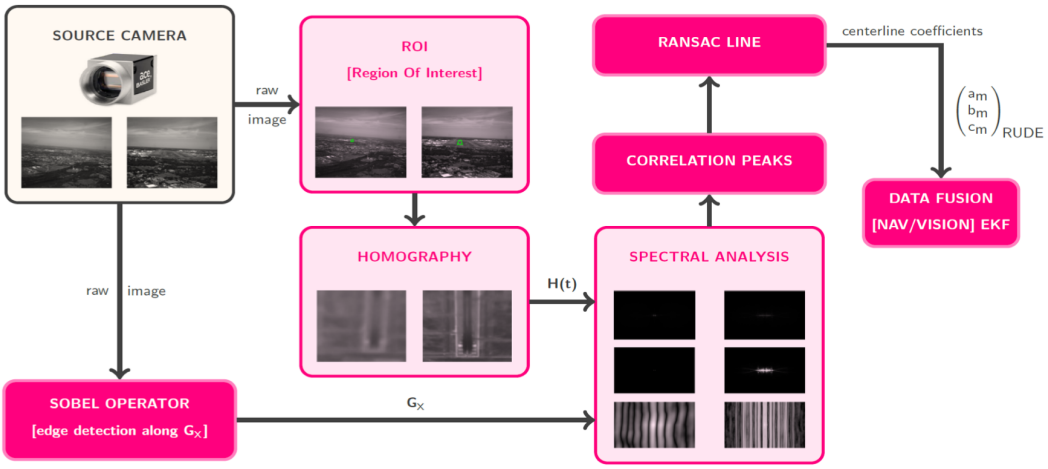

Fig. 4 Flowchart and mathematical operations performed by the Runway Detection (RuDe) algorithm

The Region Of Interest and Runway Detection (ROI+RuDe) algorithmic pipeline, represented with Fig. 4 is an adaptation of D. Dickmanns [20, 30] and K. Schertler [31] researches. ROI and RuDe algorithms are based on common image processing techniques so that ROI+RuDe pipeline combines both image area tracking (ROI) and runway center-line detection (RuDe) capabilities. The ROI algorithm is a prerequisite for RuDe to operate effectively as RuDe processes pixels over time within images that are cropped based on the picture area defined by the ROI. The ROI algorithm requires as inputs the world referenced geographic coordinates of the destination runway end point, both length and width of the destination runway, as well as its QFU61 [32]. In order to get rid of both GPS positioning measurements and A/C estimated states within the computation of the image area that surrounds the destination runway, thus preventing downstream data fusion from undesirable correlation effects, the ROI algorithm relies on a vision-based tracking technique. This tracker is firstly initialized from one GPS measurement point only before GPS sensor is turned off and an accurate enough positioning information available. After this per design initialization step, the ROI is tracked through time until destination runway threshold gets out of the image. After that, the ROI is fixed until the end of the roll-out phase. The tracking algorithm used corresponds to the MEDIANFLOW tracker of the OpenCV library. The tracking operation is not carried out by following through time the 4 edges of the parallelogram which defines the region of interest. Instead, a single MEDIANFLOW tracker is used to trace the center of the ROI every 4 image frames to alleviate the computational burden of the operation, assuming that the observed 3D scene does not significantly change during these 4 frames. To robustify the tracking solution used within ROI algorithm and prevent from too important tracker drift, two additional ROI correction mechanisms were also implemented. The first one consists in periodically comparing current computed ROI, derived from image processing, with the one obtained from the A/C estimated state components. If a significant discrepancy expressed in pixels is observed, then the ROI is reinitialized with the one computed based on the A/C estimated state. The second mechanism makes use of the runway center-line detected in the image by the RuDe algorithm to laterally reposition the ROI accordingly, assuming that this latter must be symmetric w.r.t. the detected axis.

The sequence of mathematical operations implemented in the RuDe algorithm, presented in Fig. 4, details both algorithmic flowchart and data flow that lead to the elaboration of the measurement data $\begin{pmatrix} a_m & b_m & c_m \end{pmatrix}^T$. A Sobel-Feldman filter is employed to detect edges within the processed or cropped

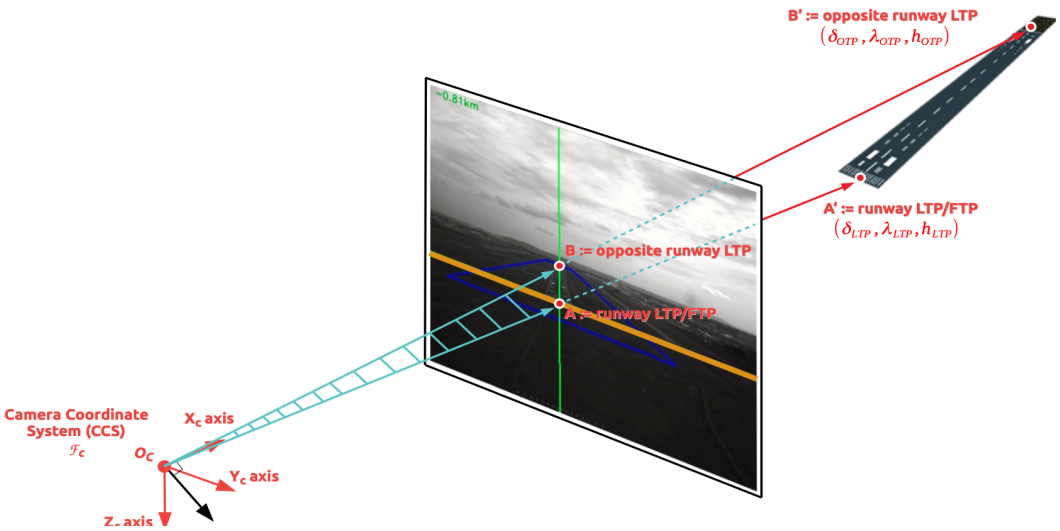

Fig. 5 Runway center-line parametrization

image. It operates as a discrete differentiator, providing an approximation of the gradient of the image intensity function. The principle of this Sobel operator is a double convolution of the image with a small, separable, and integer-valued filter in both horizontal and vertical directions. In this context, only the gradient in the horizontal direction, $\mathbf{G}_X$, is considered. While this filter imposes a relatively low CPU burden, it provides only a coarse approximation of the gradient of the image intensity function. This limitation becomes particularly evident for high-frequency variations within the observed 3D scene. From a pinhole camera model, an estimation is made of the homography of the small-sized 3D scene contained in the cropped image obtained from the computed ROI which includes the runway of destination. The estimated homography matrix, denoted as $\mathbf{H}(t)$, enables the transformation of the perspective view of the processed cropped image, effectively removing projective distortion. Then, a spectral analysis is carried out in the Fourier domain on the straightened cropped image by exploiting both pre-computed $\mathbf{G}_X$ and $\mathbf{H}(t)$ quantities. Coupling the outputs of such an analysis with the cross correlation peaks searching algorithm permits to spatially localized in the cropped image the potential axes of symmetry of the planar object under observation. The selection of the most probable right axis is then made by applying a RANSAC64 algorithm [33]. The RANSAC algorithm, employed to address a line fitting problem using a set of extracted points, produces several candidate linear models representing potential runway center-lines. Each of these models is associated with a fitness value that can be interpreted as a measure of confidence. These candidate lines are obtained by fitting multiple linear models to several data random samplings and then returning the model with the highest expectation w.r.t. a given data subset. Faced with these various options, it must be pointed out that RuDe algorithm outputs a unique line which corresponds to the one with the highest confidence level returned by the RANSAC sub-function. The RANSAC method is an iterative and non-deterministic algorithm since it outputs results featured by probabilities which increase as more iterations are allowed. Once the destination runway center-line has been extracted and identified in the image, the corresponding measurements $\begin{pmatrix} a_m & b_m & c_m \end{pmatrix}^T$ are obtained using the following mathematical parametrization:

$$\vec{n} = \frac{\overrightarrow{O_C A} \times \overrightarrow{O_C B}}{\| \overrightarrow{O_C A} \times \overrightarrow{O_C B} \|} = \begin{pmatrix} a_m \\ b_m \\ c_m \end{pmatrix}_{\mathcal{F}_C} \Rightarrow \| \vec{n} \| = \sqrt{a^2 + b^2 + c^2} \tag{2}$$

where $\times$ designates the vectorial product. The unit norm of vector $\vec{n}$ can be viewed as a constraint on the three numerical components a, b and c, so much that the normalization operation (i.e. the division by $\| \overrightarrow{O_C A} \times \overrightarrow{O_C B} \|$) is performed *a posteriori*. The proposed parametrization is adopted to shape any

line-based landmark specific of the runways. It relies on the coordinates, expressed in the Camera Coordinate System (CCS), of the unit vector that is normal to the plane containing OC, A and B, as depicted in Fig. 5. Point OC corresponds to the center of the camera, points A and B respectively refers to the image projection of the runway LTP/FTP and the opposite runway LTP. Therefore, the $(OCAB)$ plane intersects the virtual image plane at the location of the detected line. Consequently, adding vision-based measurements $\begin{pmatrix} a_m & b_m & c_m \end{pmatrix}^T$, coming from the ROI+RuDe algorithmic chain, in the data fusion process will bring only two new degrees of freedom in information processing i.e., two new dissimilar and uncorrelated measurements. This observation will also have some impact on the implementation of the sequential measurements update procedure within the EKF, as these three peculiar measurements do not respect the assumption of statistical independence.

3 Multisensor Data Fusion filter

The problem of reconstructing accurate reference inputs, DEVLOC and DEVGLD, for aircraft guidance during flight approach segment relies entirely on the knowledge of $\mathbf{r}_{\text{A/C}}^{\text{ECEF}}$ *i.e.,* the absolute position of the A/C expressed in the Earth-Centered Earth-Fixed (ECEF) frame. Thereafter, the estimation of the absolute positioning vector $\hat{\mathbf{r}}_{\text{A/C}}^{\text{ECEF}}$ is performed by means of VAEKF techniques. An augmented nonlinear state space representation of A/C navigation dynamics, denoted by $\mathcal{M}_{\text{NL}}$ in the sequel, is derived from both navigation kinematic relationships [34] and most relevant sensors errors to be estimated (*e.g.,* accelerometers/gyrometers biases, misleading cameras calibrations, air data probes inconsistencies, etc.). Such a dynamic modeling can be mathematically formulated as follows:

$$\mathcal{M}_{\text{NL}} : \begin{cases} \dot{\mathbf{X}}(t) = f(\mathbf{X}(t), \mathbf{Y}_m(t)) \\ \mathbf{Y}(t_k) = g(\mathbf{X}(t_k)) \end{cases} \tag{3}$$

Previous formulation describes a continuous-time process modeling with discrete-time output observation with $\mathbf{Y}_m$ referring to a vector of measurements. To illustrate the integration of visual measurements, the considered state vector can be formulated as: $\mathbf{X} = \begin{pmatrix} V_N & V_E & V_z & \delta_E & \lambda_E & z & \psi & \theta & \phi \end{pmatrix}^T$ and the vector of measurements is defined with Eq. 2 as $\mathbf{Y}_m = \begin{pmatrix} V_N & V_E & V_z & \delta_E & \lambda_E & z & \psi & \theta & \phi & a_m & b_m & c_m \end{pmatrix}^T$ where: $(V_N\ V_E\ V_z)$ refers to the NED velocities of the aircraft; $(\delta_E\ \lambda_E\ z)$ corresponds to its latitude, longitude and geodetic altitude (polar positioning coordinates in ECEF frame); the triplet (ψ, θ, ϕ) describes A/C attitude that is to say the orientation of the A/C body frame w.r.t. the local NED system of axes. The EKF-based estimation scheme is, a prediction step propagates both states and covariance errors to predict their future values between two discrete time-instants k and $k+1$ while a correction step corrects *a posteriori* these predictions once new measurements at time-instant $k+1$ become available. Thus, in our context, and among other possibilities, by considering that all observations (contained in vector $\mathbf{Z}_k$ in what follows with $\mathbf{Z}_k$ composed of p measurement(s) exactly with $p \in \mathbb{N}^\star$) are available at every sample period dt and futhermore, that these latter are perturbated by uncorrelated and independent noises (*i.e.,* $\forall k \in \mathbb{N}$, the estimated measurement noise covariance matrix is diagonal), the MDF filtering equation may read:

$$\hat{\mathbf{X}}_{k+1|k+1} = \hat{\mathbf{X}}_{k+1|k} + \sum_{i=1}^{p} \mathbf{K}_{k+1}^i [\mathbf{Z}_{k+1}^i - g(\hat{\mathbf{X}}_{k+1|k})] \tag{4}$$

Previous filtering equation encodes a sequential measurement update mechanism which usually prevents from ill-conditioned problem when computing correction gain matrix $\mathbf{K}$ at each time step (obtained generally by inversion of a linear system). Assuming also that the correction term remains constant over $[t_k; t_{k+1} = t_k + dt[$ for $dt << 1$, the estimated state vector at time $k+1$ can be approximated with a good

precision such that:

$$\hat{\mathbf{X}}_{k+1|k+1} \simeq \hat{\mathbf{X}}_{k|k} + f(\hat{\mathbf{X}}_{k|k}, \mathbf{Y}_m(t_k)) \cdot dt + \sum_{i=1}^{p} \mathbf{K}_{k+1}^{i} [\mathbf{Z}_{k+1}^{i} - g(\hat{\mathbf{X}}_{k+1|k})] \tag{5}$$

The previous filtering equation requires to design gains $\mathbf{K}_{k+1}^{i}$ which depend on analyzing the filtering equation (2.14) shows that the confidence that we have in the model (process equation) relatively to the one that we have in the observations. Both levels of confidence are quantified by the values in the matrices $\mathbf{Q}$ (power spectral density matrix) and $\mathbf{R}$ (covariance matrix). It is common to choose the gain that minimizes the variance of the state estimation error $\epsilon(t) = \mathbf{X}(t) - \hat{\mathbf{X}}(t)$ (corresponding estimated covariance matrix will be denoted by $\hat{\mathbf{P}}_k = E[\epsilon_k \epsilon_k^T]$. Thus, the computational steps preceding Eq. 4 are the following:

$$\begin{cases} \hat{\mathbf{X}}_{k+1|k} = \hat{\mathbf{X}}_{k|k} + \displaystyle\int_{t_k}^{t_{k+1}} f(\mathbf{X}(t), \mathbf{Y}_m(t_k)) dt & \text{(6a)} \\ \mathbf{K}_{k+1} = \hat{\mathbf{P}}_{k+1|k} \mathbf{C}_k^T \left(\mathbf{C}_k \hat{\mathbf{P}}_{k+1|k} \mathbf{C}_k^T + \mathbf{R}_k \right)^{-1} & \text{(6b)} \\ \hat{\mathbf{P}}_{k+1|k} \approx \Phi_{k+1} \hat{\mathbf{P}}_{k|k} \Phi_{k+1}^T + \mathbf{Q}(t_k) dt & \text{(6c)} \\ \Phi_{k+1} = e^{\mathbf{A}_k} \approx \mathbf{I} + \mathbf{A}_k dt + (\mathbf{A}_k dt)^2/2! & \text{(6d)} \\ \mathbf{C}_k = \left. \dfrac{\partial g(\mathbf{X}(t))}{\partial \mathbf{X}} \right|_{\mathbf{X}(t)=\hat{\mathbf{X}}_{k+1|k}} & \text{(6e)} \\ \mathbf{A}_k = \left. \dfrac{\partial f(\mathbf{X}(t), \mathbf{Y}_m(t_k))}{\partial \mathbf{X}} \right|_{\mathbf{X}(t)=\hat{\mathbf{X}}_{k|k}} & \text{(6f)} \end{cases}$$

Once these theoretical estimation principles have been stated, VAEKF algorithms can be designed and implemented for merging an heterogeneous set of simulated measurements $\mathbf{Z}$ comprising GPS/GNSS data, IMU measurements, air data flight parameters etc. but also, and above all, vision-based information such as the one previously presented with the RuDe image processing algorithm. The prediction associated with the vision measurements is computed with Eq. 2. The key point is that both points A and B (cf. Fig. 5) correspond to known mapped locations available in the navigation database. Therefore, the Cartesian coordinates of these points w.r.t. the ECEF frame can be immediately calculated. Then, the successive and multiple changes of coordinates between ECEF, local NED, aircraft body and camera frames (assuming a pinhole camera model) allow to deduce the coordinates of both $\overrightarrow{O_C A'}$ and $\overrightarrow{O_C B'}$ vectors in the camera frame, $\mathcal{F}_C$. The coordinates of the runway LTP can be written in a compact form of the whole change of coordinates in function of estimated A/C state as:

$$\mathbf{X}_C^{LTP} = -\mathbf{M}_{C\to B}^{rot} \left(\mathbf{M}_{N\to B}^{rot}\{\psi, \theta, \phi\} \mathbf{M}_{E\to R'}^{LTP}\{\delta_{LTP}, \lambda_{LTP}\} \left(\mathbf{X}_E^{CoM}\{\delta_E, \lambda_E, h\} - \mathbf{X}_E^{LTP} \right) + \mathbf{T}_B \right) \tag{7}$$

with $\mathbf{X}_E^{CoM}$ and $\mathbf{X}_E^{LTP}$ respectively the ECEF coordinates of the A/C Center of Mass (CoM) and the runway LTP defined as:

$$\begin{cases} \mathbf{X}_E^{CoM} = \begin{pmatrix} (N(\delta_E) + h) \cos\delta_E \cos\lambda_E \\ (N(\delta_E) + h) \cos\delta_E \sin\lambda_E \\ \left(N(\delta_E)(1+e^2) + h\right) \sin\delta_E \end{pmatrix} & \text{(8a)} \\ \mathbf{X}_E^{LTP} = \begin{pmatrix} (N(\delta_{LTP}) + h) \cos\delta_{LTP} \cos\lambda_{LTP} \\ (N(\delta_{LTP}) + h) \cos\delta_{LTP} \sin\lambda_{LTP} \\ \left(N(\delta_{LTP})(1+e^2) + h\right) \sin\delta_{LTP} \end{pmatrix} & \text{(8b)} \end{cases}$$

$\mathbf{M}^{LTP}_{E\to R'}\{\delta_{LTP}, \lambda_{LTP}\}$ is the constant rotation matrix between the ECEF and the runway geographic frame, R', given by:

$$\mathbf{M}^{LTP}_{E\to R'}\{\delta_{LTP}, \lambda_{LTP}\} = \begin{bmatrix} -\sin\delta_{LTP}\cos\lambda_{LTP} & -\sin\delta_{LTP}\sin\lambda_{LTP} & \cos\lambda_{LTP} \\ -\sin\lambda_{LTP} & \cos\lambda_{LTP} & 0 \\ -\cos\delta_{LTP}\cos\lambda_{LTP} & -\cos\delta_{LTP}\sin\lambda_{LTP} & -\sin\delta_{LTP} \end{bmatrix} \tag{9}$$

$\mathbf{M}^{rot}_{N\to B}\{\psi, \theta, \phi\}$ represents the rotation matrix that relates the A/C local NED frame to the A/C body frame, as detailed in [35]. This matrix depends on the estimated states of the aircraft. Lastly, $\mathbf{M}^{rot}_{C\to B}$ and $\mathbf{T}_B$ denote the fixed rotation matrix and translation vector between the A/C body frame and the CCS, respectively. The coordinates of point B', the Opposite Threshold Point (OTP), are obtained with similar operations. Applying Eq. 2 to $\mathbf{X}^{LTP}_C$ and $\mathbf{X}^{OTP}_C$ with the normalization of the cross product provides the predicted output $\begin{pmatrix} \hat{a}_{k+1|k} & \hat{b}_{k+1|k} & \hat{c}_{k+1|k} \end{pmatrix}^T$ which can be compared with the measurements issued by the ROI+RuDe pipeline. The general structure of the measurement Jacobian matrix $\mathbf{C}$, Eq. 6e, is increased with the derivation of $\vec{n}$ for each states x of the previously defined vector $\mathbf{X}$ such that:

$$\frac{\partial \vec{n}}{\partial x} = \frac{1}{D_{\|.\|}} \frac{\partial}{\partial x}(\mathbf{X}^{LTP}_C \times \mathbf{X}^{OTP}_C) - \frac{1}{D^3_{\|.\|}} \left((\mathbf{X}^{LTP}_C \times \mathbf{X}^{OTP}_C)^T \frac{\partial}{\partial x}(\mathbf{X}^{LTP}_C \times \mathbf{X}^{OTP}_C) \right) (\mathbf{X}^{LTP}_C \times \mathbf{X}^{OTP}_C) \tag{10}$$

with $D_{\|.\|} = \|\mathbf{X}^{LTP}_C \times \mathbf{X}^{OTP}_C\|$. At this stage, this extra vision-based information can be merged to correct A/C predicted state $\hat{X}_{k+1|k}$ within data fusion process.

4 Implementation of the control architecture

The PBVS strategy is validated by performing various landings on a high-fidelity real-time simulation platform developed at ONERA [28]. The software/hardware architecture has been implemented to guarantee tight and high-fidelity coupling between flight dynamics and visual environment models, allowing for state observation, computer vision processing, virtual sensor data fusion and full aircraft control. A Boeing 747 mathematical model, [36], is chosen as use case for the simulation environment and implemented on the real-time programming unit. The simulator operates by generating a synthetic video stream with Microsoft Flight Simulator 2020 on a computing unit, coupled to the real-time aircraft pose evolution streamed by a Speedgoat real-time machine, while a second computing unit captures the images and executes the MDF layer. Due to the lack of real flight data with a Boeing 747, each autonomous vision-based landings are compared to nominal landings. A nominal landing consists in performing, on the simulation platform, an autonomous landing with ILS autopilots fed by position measurements. The PBVS strategy is initially demonstrated through landings on the two runways (32L and 32R) of Toulouse's airport (LFBO). In a subsequent endeavor, the sensitivity of the system to different lighting conditions is addressed.

4.1 Guidance control

Every landing starts with GPS/GNSS measurements, which in the absence of sensor models corresponds to the exact A/C position issued by the modeled dynamics, to initialize the ROI+RuDe algorithms. A switch to a vision-based landing occurs when the runway is detected on the image with enough pixels. In the GPS/GNSS initialization phase, the A/C is guided with altitude and thrust control while beginning to align with the runway by capturing the lateral deviation signal. Upon incorporating vision measurements, the A/C transitions to tracking and capturing both deviations, along with maintaining Indicated Airspeed, V_{IAS}, tracking. The pre-vision-based control is traduced by the following guidance

laws feeding A/C inner loops, i.e. pitch, roll and thrust, defined as [37]:

$$\begin{cases} \phi_d = \mathbf{K}_\phi \mathsf{DEVLOC} + \mathbf{D}_\phi \dot{\mathsf{DEVLOC}} & \text{(11a)} \\ \theta_d = \mathbf{K}_\theta \left(Z_d - Z\right) + \mathbf{D}_\theta \left(V_{Z_d} - V_Z\right) & \text{(11b)} \\ u_{thr_d} = u_{thr_{trim}} & \text{(11c)} \end{cases}$$

with $u_{thr_{trim}}$ the necessary thrust to maintain a desired NED altitude, Z_d. $\mathbf{K}_\theta$, $\mathbf{K}_\phi$ and $\mathbf{D}_\theta$, $\mathbf{D}_\phi$ are respectively the constant proportional and derivative gains for the longitudinal/lateral guidance laws. When the ROI+RuDe provides a validity of the visual measurements, the guidance laws are fed by the estimated lateral and longitudinal deviations computed by the VAEKF. These last become [37]:

$$\begin{cases} \phi_d = \mathbf{K}_\phi \mathsf{DEVLOC} + \mathbf{D}_\phi \dot{\mathsf{DEVLOC}} & \text{(12a)} \\ \theta_d = -\mathbf{K}_\theta \mathsf{DEVGLD} + \mathbf{D}_\theta \dot{\mathsf{DEVGLD}} + \sigma_H \left(\mathbf{K}_{flare}\delta_g + \mathbf{D}_{flare}\dot{\delta}_g\right) & \text{(12b)} \\ \sigma_H = \begin{cases} 1 & \text{if } \delta_g \leq \delta_{flare} \\ 0 & \text{otherwise} \end{cases} & \text{(12c)} \\ u_{thr_d} = \mathbf{K}_u \left(V_{IAS_d} - V_{IAS}\right) + \mathbf{D}_u \left(\dot{V}_{IAS_d} - \dot{V}_{IAS}\right) & \text{(12d)} \end{cases}$$

with $\mathbf{K}_.$ and $\mathbf{D}_.$ are respectively constant proportional and derivative gains. A flare phase is implemented in the longitudinal guidance law with the term σ_H in Eq. (12b). δ_g represents the distance to the ground, while δ_{flare} signifies the distance to initiate the flare maneuver, which is typically set at 50 feet above the LTP. Different capturing and tracking dynamics of the lateral and longitudinal deviations are imposed to deal with external disturbances such as crosswinds [38].

In the event of a loss or failure in runway detection using the ROI+RuDe algorithms, the validity signal prompts a switch back to available measurements. This means that the landing continues with Eq. 12, which are fed by ground-truth deviations.

4.2 Performance evaluation through landings on a real-time simulation platform

Condition #	C1	C2	C3
Longitude, Latitude (°)	43.619, 1.3721	43.4723, 1.5318	43.5131, 1.4825
Altitude - wgs (ft)	3087	3355	3310
ϕ, θ, ψ (°)	1.45, -7.03, -24.4	3.88, 25.16, -62.33	1.6, -1, -37.2
$\dot{\phi}, \dot{\theta}, \dot{\psi}$ (°/s)	-0.29, -1.12, -0.49	0.76, -3.15, 0	-0.2, 2, 0
Flight Path Angle (°)	1.453	0	0.9
Speed (kts)	240	260	260

Table 1 Boeing 747 initial flying conditions for landings in Toulouse airport (LFBO)

All initial conditions employed for landing simulations, on both LFBO runways, correspond to realistic data from real flight and are provided in Tab. 1. For these flights, the simulation platform is configured to depict a bright, sunny day with the time set at noon as illustrated by Fig. 6. Fig. 7a and 7b provide a graphical representation of the 3D trajectories for the vision-based landings, juxtaposed with their respective nominal trajectories. Approximately 12 km from the LTPs, the ROI+RuDe algorithms initiate the detection of the runway of interest in the image. Fig. 6 offers a visual representation of the ROI, depicted as a blue parallelepiped, alongside the center-line represented by a green line. As a result, the VAEKF outputs continue to provide guidance commands throughout the touchdown phase, ensuring that the runway remains visible in the image throughout the entire process. Upon initial examination, the

autonomous vision-based landings (illustrated with dashed lines) effectively replicate the performance of an ILS-like autonomous landing with ground-truth measurements (depicted with solid lines). This finding is corroborated by the analysis of DEVLOC and DEVGLD deviations, as shown with Fig. 8 and 9. Fig. 10 presents the corresponding errors against the ground-truth actual deviations of all landings. The lateral error, DEVLOC, has a zero mean distribution and a standard deviation of about 0.1 m, while the vertical error, DEVGLD has a 0.8 m mean and a 0.7 m standard deviation. While lower performance levels are observed for aircraft positioned beyond a distance of 10 km from the runway, it is noteworthy that, as demonstrated in the comparison shown in Fig. 8 and 9, the estimation performances remain acceptable. They closely align with the behaviors achieved using ground-truth measurements.

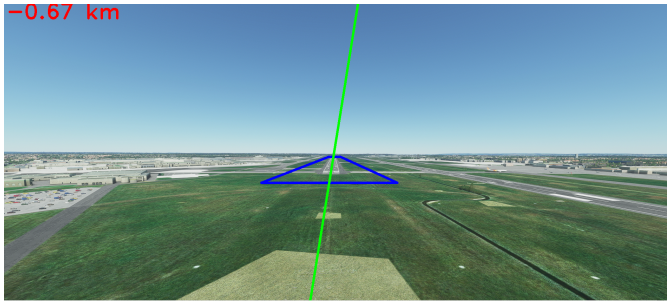

Fig. 6 Illustration of ROI+RuDe outputs on the MSFS world rendering of Toulouse's airport.

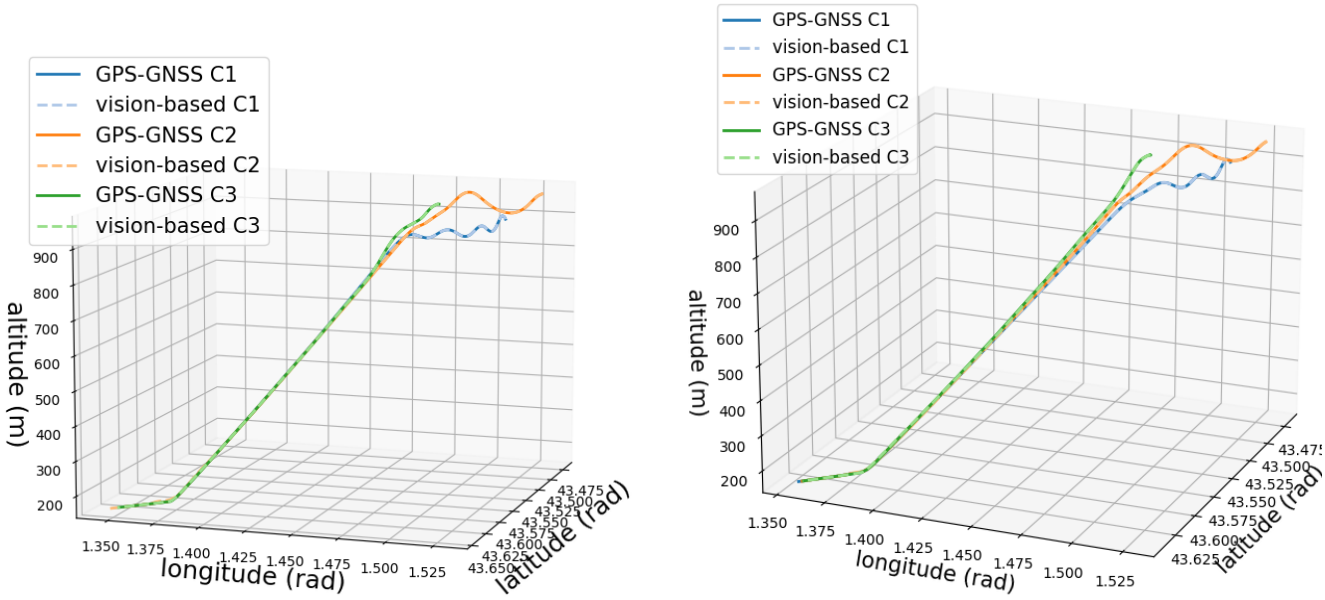

(a) 3D trajectories for landings on LFBO 32L

(b) 3D trajectories for landings on LFBO 32R

Fig. 7 Comparison of 3D trajectories between ILS landings with GPS-GNSS (full-line) and vision-based landings (dashed-line) performed on SCHEMIN for the initial conditions listed in Tab. 1.

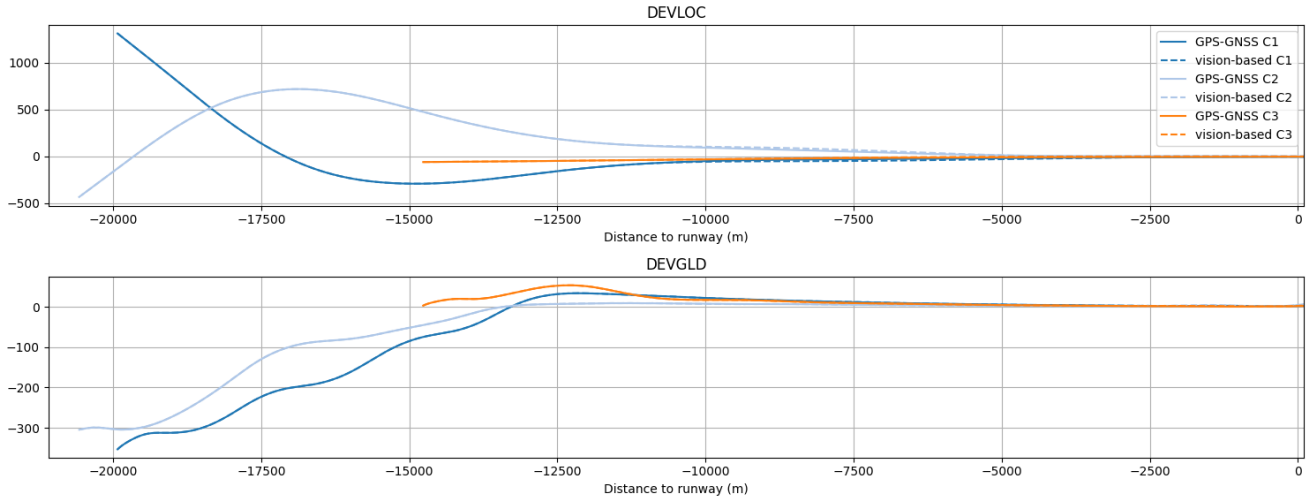

Fig. 8 Comparison of estimated deviations DEVLOC (top subplot) and DEVGLD (bottom subplot) in function of the distance to the runway LTP for landings on LFBO 32L initialized with conditions in Tab. 1.

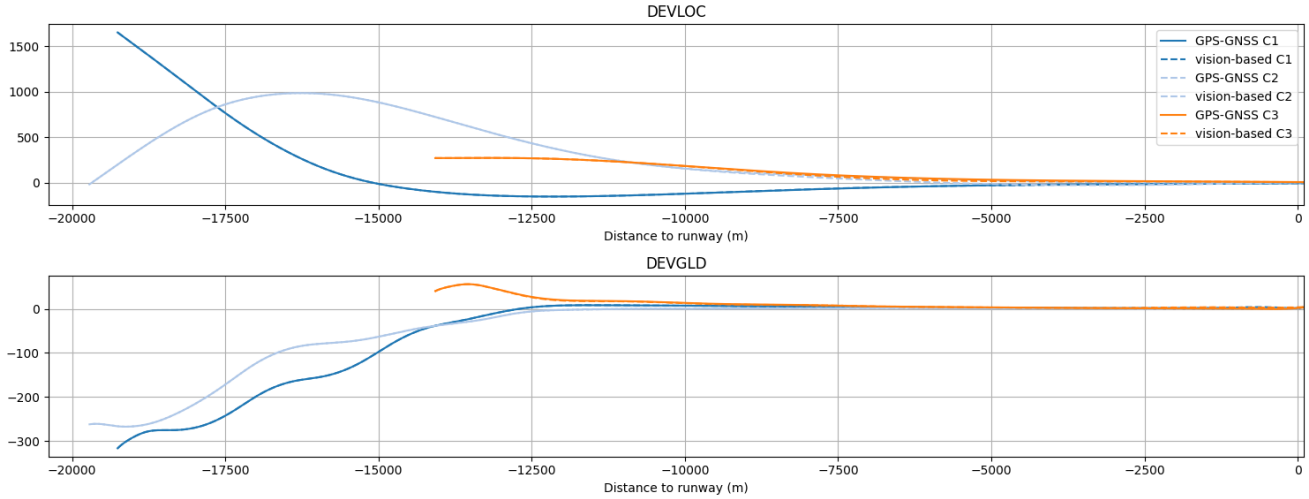

Fig. 9 Comparison of estimated deviations DEVLOC (top subplot) and DEVGLD (bottom subplot) in function of the distance to the runway LTP for landings on LFBO 32R initialized with conditions in Tab. 1.

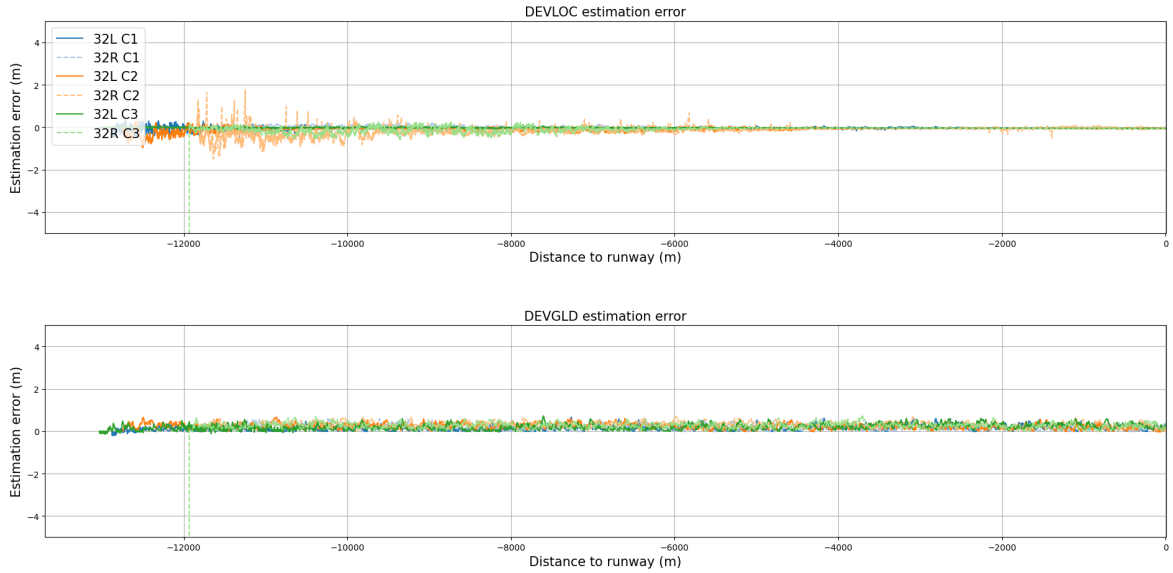

Fig. 10 Estimation error of DEVLOC (top subplot) and DEVGLD (bottom subplot) in function of the distance to the runway LTP for landings initialized with conditions in Tab. 1.

4.3 Sensitivity to visual conditions

As demonstrated in open-loop validation tests conducted in [28], it is evident that lighting conditions have an impact on the performance of the VAEKF. Therefore, it is imperative to conduct autonomous landings under various weather conditions to validate the proposed control framework. To that aim,landings are executed under the visual conditions illustrated in Fig. 12. All flights are initiated with condition C1, detailed in Tab. 1, with the aim of landing on runway 32L. Additionally to illustrate the variety of the visual environment and the different brightness, Fig. 12 demonstrates the accuracy of the ROI+RuDe pipeline at 1.5km from the LTP. Upon reviewing the comparison of 3D trajectories for autonomous vision-based landings against a nominal trajectory depicted in Fig. 11, an initial observation reveals similar performance levels. Fig. 14 confirms the generally consistent behavior of the CV algorithms with respect to the evolution of the center-line parameters. Notably, in conditions of lower image brightness, performance degrades as the aircraft approaches the runway. This trend is also evident in Fig. 13, which highlights a slower lateral dynamic for darker images. This behavior can be attributed to Fig. 15, which illustrates that image brightness affects estimation accuracy, particularly when the aircraft is further from the runway. In such cases, errors of nearly 2m are observed, impacting the inherently sluggish lateral dynamics of the Boeing 747. In conclusion, despite

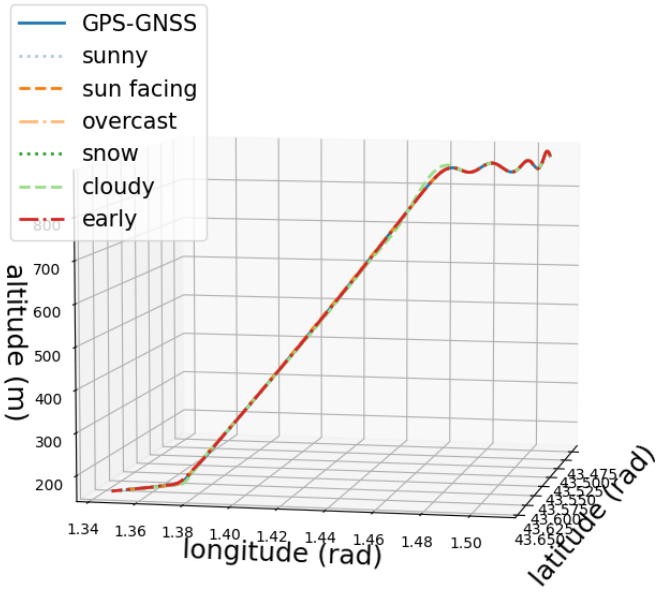

Fig. 11 3D trajectories of vision-based landings, alongside nominal trajectory at LFBO 32L, for different weather and at C1 initial conditions.

the sensitivity of the ROI+RuDe algorithms to image brightness, the VAEKF proves to be capable of providing satisfactory estimates of the lateral and longitudinal deviations under the considered weather conditions. In cases of more challenging image illumination, this may lead to a slower capture of the lateral deviation signal and potentially result in a touchdown with a minor offset from the center-line, typically less than 3m, as demonstrated in Figure 13 for a runway width of 45 meters.

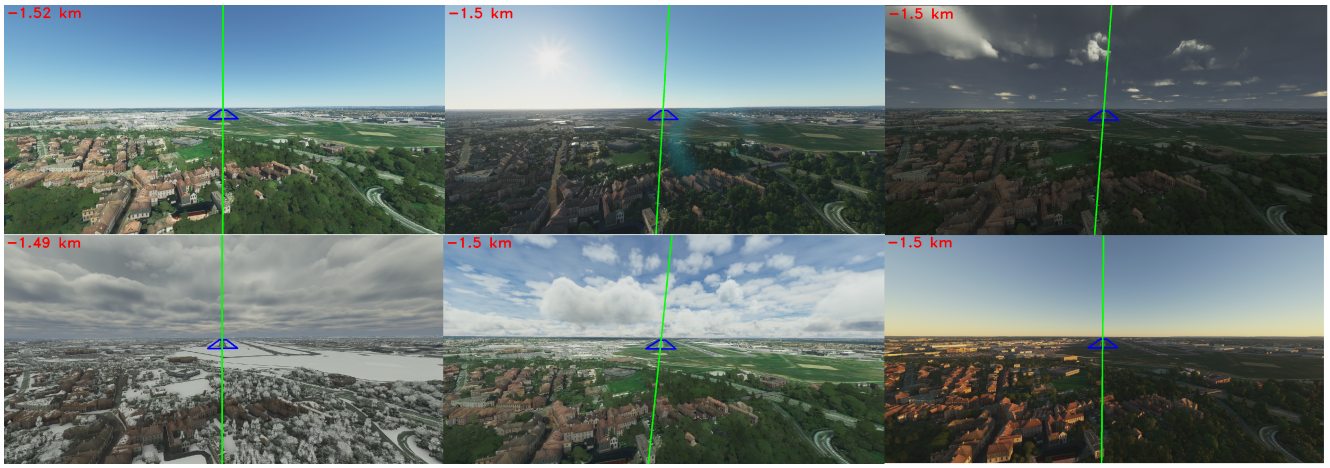

Fig. 12 Illustration of ROI+RuDe outputs for different weather conditions. From top-left clockwise: clear, sun-facing, overcast, early, cloudy, snowy.

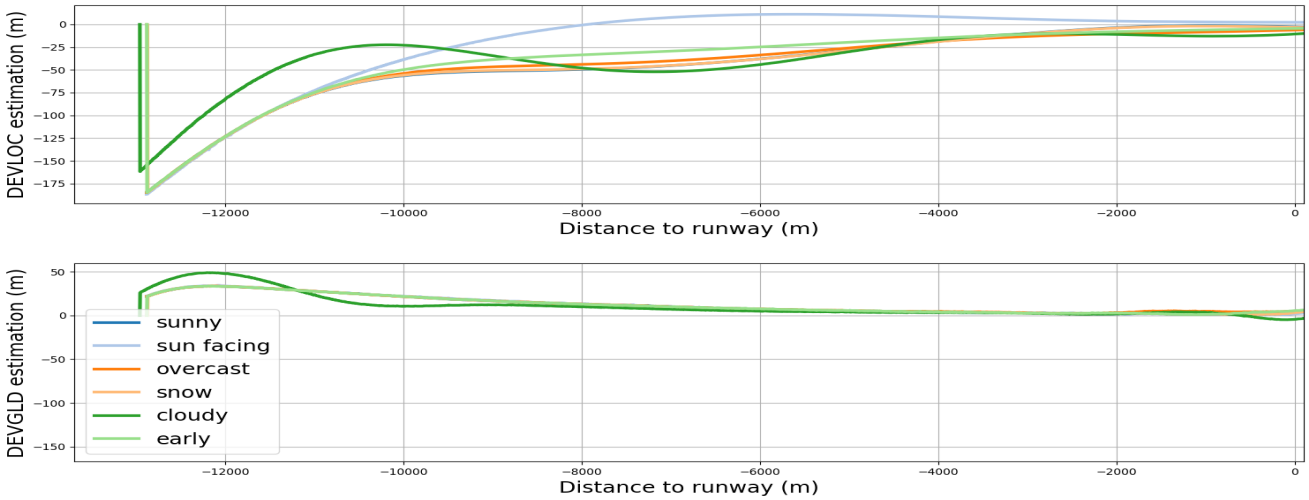

Fig. 13 Comparison of estimated deviations DEVLOC (top subplot) and DEVGLD (bottom subplot) in function of the distance to the runway LTP.

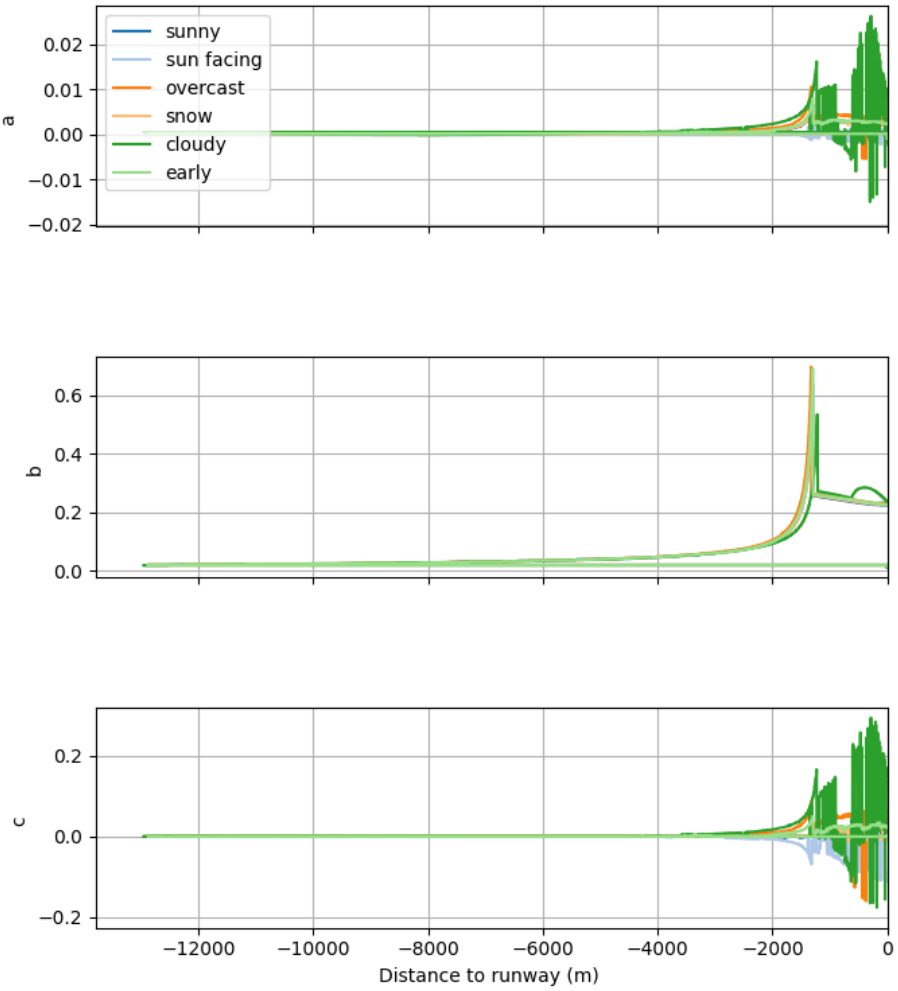

Fig. 14 Center-line parameters not normalized, Eq. 2, in function of the distance to the runway LTP for visual conditions depicted in Fig. 12.

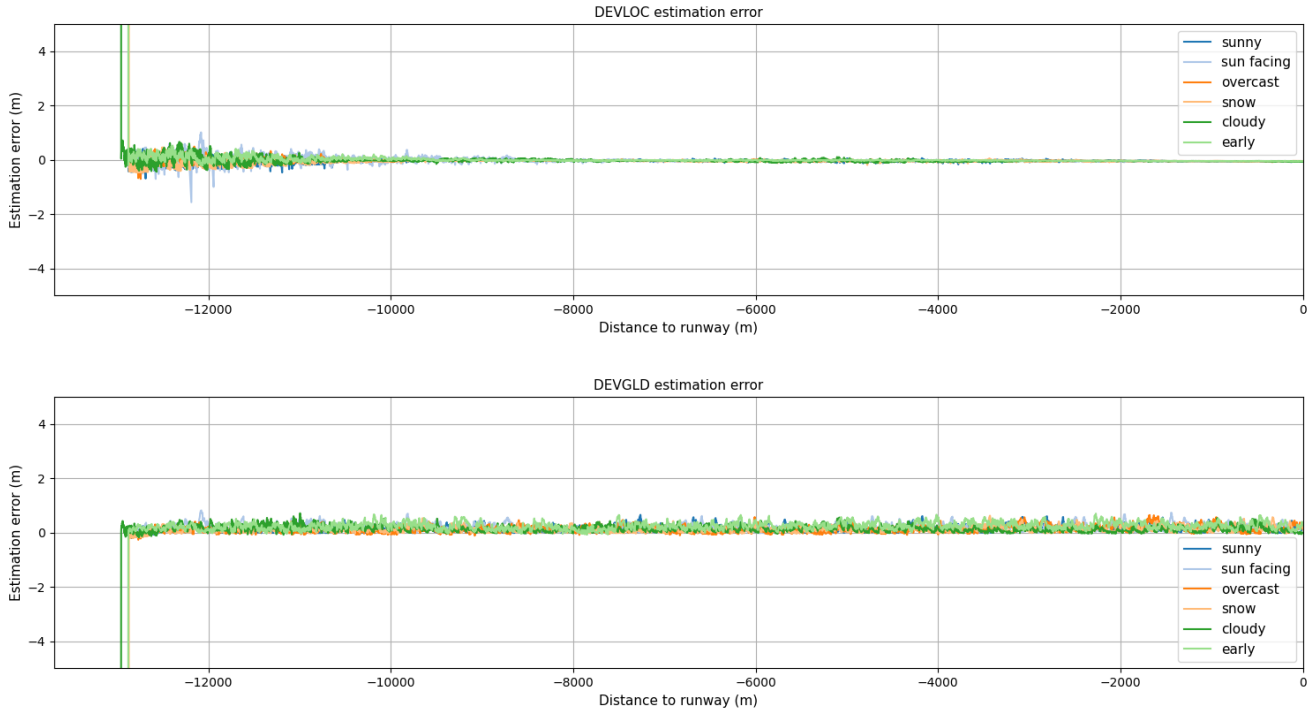

Fig. 15 Estimation error of DEVLOC (top subplot) and DEVGLD (bottom subplot) in function of the distance to the runway LTP for visual conditions depicted in Fig. 12.

5 Conclusion

To conclude, this paper presented a novel Pose-Based Visual Servoing strategy for autonomous approach and landing of an airliner. The proposed architecture is decomposed in an ILS-like guidance law supplied by an original vision-based multi-sensor data fusion for the aircraft's lateral and longitudinal deviations calculation w.r.t. the runway center-line. The integration of the runway center-line paramatrization for the aircraft pose estimation is another key contribution of the presented study. To highlight the interest and the feasibility of the novel control scheme, extensive tests have been carried out on a highly realistic simulation platform available at ONERA. Results demonstrated the relevance of the proposed vision-based control strategy for civil aviation autonomous functions in forthcoming future.

Future work will focus on robustifying the control law and parameters estimation against external perturbations and sensor's fault. Likewise, runway detection with artificial neural networks and machine learning strategies will be investigated to reduce the use of geographical knowledge information.

References

[1] Carl Milner, Christophe Macabiau, Arielle Gantelet, Shreyas Prakasen, N Tairo C Manase, L Azoulai, and F Tranchet. Modelling of egnos navigation system errors for cat i autoland. In *Proceedings of the 35th International Technical Meeting of the Satellite Division of The Institute of Navigation (ION GNSS+ 2022)*, pages 1496–1513, 2022. DOI: 10.33012/2022.18422.

[2] Pascal Traverse, Isabelle Lacaze, and Jean Souyris. Airbus fly-by-wire: A total approach to dependability. In *Building the Information Society: IFIP 18th World Computer Congress Topical Sessions 22–27 August 2004 Toulouse, France*, pages 191–212. Springer, 2004. DOI: 10.1007/978-1-4020-8157-6_18.

[3] François Chaumette and Seth Hutchinson. Visual servo control. i. basic approaches. *IEEE Robotics & Automation Magazine*, 13(4):82–90, 2006. DOI: 10.1109/MRA.2006.250573.

[4] William J Wilson, CC Williams Hulls, and Graham S Bell. Relative end-effector control using cartesian position based visual servoing. *IEEE Transactions on Robotics and Automation*, 12(5):684–696, 1996. DOI: 10.1109/70.538974.

[5] Patrick Rives. Visual servoing based on epipolar geometry. In *Proceedings. 2000 IEEE/RSJ International Conference on Intelligent Robots and Systems (IROS 2000)(Cat. No. 00CH37113)*, volume 1, pages 602–607. IEEE, 2000. DOI: 10.1109/IROS.2000.894670.

[6] Odile Bourquardez and François Chaumette. Visual servoing of an airplane for alignment with respect to a runway. In *Proceedings 2007 IEEE International Conference on Robotics and Automation*, pages 1330–1335. IEEE, 2007. DOI: 10.1109/ROBOT.2007.363169.

[7] Najib Metni, Tarek Hamel, and Isabelle Fantoni. Visual servoing with orientation limits of a x4-flyer. In *2003 European Control Conference (ECC)*, pages 1804–1809. IEEE, 2003. DOI: 10.23919/ECC.2003.7085227.

[8] Henry de Plinval and Laurent Burlion. Nonlinear visual servoing control for vtol uavs with field of view constraint. In *Advances in Aerospace Guidance, Navigation and Control: Selected Papers of the Third CEAS Specialist Conference on Guidance, Navigation and Control held in Toulouse*, pages 531–548. Springer, 2015. DOI: 10.1007/978-3-319-17518-8$_3$1.

[9] Bruno Herisse, Francois-Xavier Russotto, Tarek Hamel, and Robert Mahony. Hovering flight and vertical landing control of a vtol unmanned aerial vehicle using optical flow. In *2008 IEEE/RSJ International Conference on Intelligent Robots and Systems*, pages 801–806. IEEE, 2008. DOI: 10.1109/IROS.2008.4650731.

[10] Antoine Beyeler, Jean-Christophe Zufferey, and Dario Floreano. Vision-based control of near-obstacle flight. *Autonomous robots*, 27(3):201–219, 2009. DOI: 10.1007/s10514-009-9139-6.

[11] Patrick Rives and José R Azinheira. Linear structures following by an airship using vanishing point and horizon line in a visual servoing scheme. In *IEEE International Conference on Robotics and Automation, 2004. Proceedings. ICRA'04. 2004*, volume 1, pages 255–260. IEEE, 2004. DOI: 10.1109/ROBOT.2004.1307160.

[12] José Raul Azinheira and Patrick Rives. Image-based visual servoing for vanishing features and ground lines tracking: Application to a uav automatic landing. *International Journal of Optomechatronics*, 2(3):275–295, 2008. DOI: 10.1080/15599610802303314.

[13] Odile Bourquardez. *Commande d'engins volants par asservissement visuel*. PhD thesis, Université Rennes 1, 2008.

[14] Florent Le Bras, Tarek Hamel, Christian Barat, and Robert Mahony. Nonlinear image-based visual servo controller for automatic landing guidance of a fixed-wing aircraft. In *2009 European Control Conference (ECC)*, pages 1836–1841. IEEE, 2009. DOI: 10.23919/ECC.2009.7074670.

[15] Pedro Serra, Rita Cunha, Tarek Hamel, Carlos Silvestre, and Florent Le Bras. Nonlinear image-based visual servo controller for the flare maneuver of fixed-wing aircraft using optical flow. *IEEE Transactions on Control Systems Technology*, 23(2):570–583, 2014. DOI: 10.1109/CDC.2010.5717829.

[16] Laurent Coutard, François Chaumette, and Jean-Michel Pflimlin. Automatic landing on aircraft carrier by visual servoing. In *2011 IEEE/RSJ International Conference on Intelligent Robots and Systems*, pages 2843–2848. IEEE, 2011. DOI: 10.1109/IROS.2011.6094887.

[17] Gibert Victor and Puyou Guilhem. Landing of an airliner using image based visual servoing. *IFAC Proceedings Volumes*, 46(23):74–79, 2013. DOI: 10.3182/20130904-3-FR-2041.00103.

[18] ED Dickmanns. 4 d-dynamic scene analysis with integral spatio-temporal models. In *Proceedings of the 4th international symposium on Robotics Research*, pages 311–318, 1988.

[19] Simon Fürst, Stefan Werner, Dirk Dickmanns, and Ernst Dieter Dickmanns. Landmark navigation and autonomous landing approach with obstacle detection for aircraft. In *Enhanced and Synthetic Vision 1997*, volume 3088, pages 28–39. SPIE, 1997. DOI: 10.1117/12.277242.

[20] Dirk Dickmanns, Josep Boada, Victor Gibert, and Falk Schubert. Vision based landing for commercial aircraft. In *6th EUROPEAN CONFERENCE FOR AEROSPACE SCIENCES*, 2015.

[21] Victor Gibert, Franck Plestan, Laurent Burlion, J Boada-Bauxell, and Abdelhamid Chriette. Visual estimation of deviations for the civil aircraft landing. *Control engineering practice*, 75:17–25, 2018. DOI: 10.1016/j.conengprac.2018.03.004.

[22] Victor Gibert. *Analyse d'observabilité et synthèse d'observateurs robustes pour l'atterrissage basé vision d'avions de ligne sur des pistes inconnues*. PhD thesis, UNIVERSITE NANTES ANGERS LE MANS, 2016.

[23] Yoko Watanabe, Augustin Manecy, Antal Hiba, Sho Nagai, and Shin Aoki. Vision-integrated navigation system for aircraft final approach in case of gnss/sbas or ils failures. In *AIAA Scitech 2019 Forum*, page 0113, 2019. DOI: 10.2514/6.2019-0113.

[24] Kejun Shang, Xixi Li, Chongliang Liu, Li Ming, and Guangfeng Hu. An integrated navigation method for uav autonomous landing based on inertial and vision sensors. In *Artificial Intelligence: Second CAAI International Conference, CICAI 2022, Beijing, China, August 27–28, 2022, Revised Selected Papers, Part II*, pages 182–193. Springer, 2023. DOI: 10.1007/978-3-031-20500-2_15.

[25] Evan Kawamura, Chester Dolph, Keerthana Kannan, Thomas Lombaerts, and Corey A Ippolito. Simulated vision-based approach and landing system for advanced air mobility. In *AIAA SciTech 2023 Forum*, page 2195, 2023. DOI: 10.2514/6.2023-2195.

[26] Maik Angermann, Stephan Wolkow, Andreas Dekiert, Ulf Bestmann, and Peter Hecker. Fusion of dual optical position solutions for augmentation of gnss-based aircraft landing systems. In *Proceedings of the 2019 International Technical Meeting of The Institute of Navigation*, pages 283–295, 2019. DOI: 10.33012/2019.16694.

[27] Tamás Gróf, Péter Bauer, and Yoko Watanabe. Positioning of aircraft relative to unknown runway with delayed image data, airdata and inertial measurement fusion. *Control Engineering Practice*, 125:105211, 2022. DOI: 10.1016/j.conengprac.2022.105211.

[28] Sofiane Kraïem, Mario Cassaro, Cédric Seren, Aurélien Plyer, Gustav Öman Lundin, and Mathieu Brunot. Schemin a simulation environment for aircraft vision-based autonomous landing system design and testing. In *2024 10th International conference on automation, robotics and applications (ICARA)*. IEEE, 2024.

[29] Radio Technical Commission for Aeronautics. Do-253d, minimum operational performance standards for gps local area augmentation system airborne equipment. 2008.

[30] Ernst Dieter Dickmanns. *Dynamic vision for perception and control of motion*. Springer Science & Business Media, 2007. DOI: 10.1007/978-1-84628-638-4.

[31] Klaus Schertler. Method and device for image-assisted runway localization, Feb. 14 2017. US Patent 9,569,668.

[32] J Manjon-Sanchez, N Torres-Matabosch, F Gianni, A Plyer, and C Seren. Attol landing fdd, issue 4.0. In *ATTOL Demonstrator Project, AIRBUS UpNext Functional Description Document referenced V22RP1920756*, 2020.

[33] Martin A Fischler and Robert C Bolles. Random sample consensus: a paradigm for model fitting with applications to image analysis and automated cartography. *Communications of the ACM*, 24(6):381–395, 1981. DOI: 10.1145/358669.358692.

[34] Brian L Stevens, Frank L Lewis, and Eric N Johnson. *Aircraft control and simulation: dynamics, controls design, and autonomous systems*. John Wiley & Sons, 2015.

[35] Richard E McFarland. A standard kinematic model for flight simulation at nasa ames. Technical report, NASA, 1975.

[36] Mario Cassaro, Paolo Gunetti, Manuela Battipede, and Piero Gili. Overview of the multipurpose aircraft simulation laboratory experience. In *2013 Aviation Technology, Integration, and Operations Conference*, page 4306, 2013. DOI: 10.2514/6.2013-4306.

[37] Paolo Gunetti, Mario Cassaro, Manuela Battipede, and Piero Gili. Modeling autopilot suites for a multi-aircraft simulator. In *AIAA Modeling and Simulation Technologies (MST) Conference*, page 4736, 2013. DOI: 10.2514/6.2013-4736.

[38] JM Biannic, C Roos, and J Lesprier. Nonlinear structured h controllers for parameter-dependent uncertain systems with application to aircraft landing. *Aerospace Lab*, (13):pages–1, 2017. DOI: 10.1109/CCA.2014.6981384.